Applied Catalysis B: Environmental 182 (2016) 74–84

Contents lists available at ScienceDirect

Applied Catalysis B: Environmental

journal homepage: www.elsevier.com/locate/apcatb

Synergetic effects of plasma and metal oxide catalysts on diesel soot oxidation

Hadi Ranji-Burachaloo, Saghar Masoomi-Godarzi, Abbas Ali Khodadadi*, Yadollah Mortazavi**

Catalysis and Nanostructured Materials Laboratory, School of Chemical Engineering, College of Engineering, University of Tehran, Tehran, Iran

ARTICLE INFO

Article history:
Received 16 June 2015
Received in revised form 2 September 2015
Accepted 8 September 2015
Available online 11 September 2015

Keywords:
Diesel soot
Oxidation
Plasma
Metal oxide
Catalyst

ABSTRACT

The synergetic effects of a pin-to-plate corona plasma and Mn, Co and Fe oxide catalysts on soot oxidation were investigated under diesel exhaust gas conditions of 10% oxygen and 180–350 °C. The catalysts were synthesized by a precipitation method and characterized by XRD, BET surface area, SEM, EDX mapping, and temperature programmed methods of H_2-reduction, O_2-desorption and oxidation. The effects of energy injection, gas temperature, NO_x, and water vapor were investigated on the soot removal efficiency in the absence and presence of catalysts. Both tight and in-situ catalyst–soot contacts were examined. NO_x as the most hazardous pollutant in the diesel exhaust gas is completely removed in plasma. In the presence of the catalyst, the soot removal efficiency and selectivity to CO_2 enhance by up to 77 and 29%, respectively, as compared to those in the plasma alone. The highest removal efficiency and CO_2 selectivity are obtained on manganese and iron oxides at high and low temperatures, respectively. 49.3 and 17.4% enhancements of energy efficiency are observed, when 3.5% H_2O vapor or 450 ppm NO_x is added to the plasma–MnO_x catalysis system at 5.7 W and 300 °C, respectively. High energy efficiencies at very low energy injections are the advantages of this study.

1. Introduction

Diesel engines are the most effective combustion motors used for a wide range of automotive and technical applications. However, diesel engines emit diesel exhaust particulates (DEP) basically composed of soot derived from incomplete combustion with serious problems for human health and environment [1]. Emission regulations for DEP have become increasingly stringent globally. Therefore, it is necessary to develop effective technologies for the DEP pollutant removal [2]. Diesel particulate filter (DPF) with different designs is used as the most common method to remove DEP [3]. DPFs operate in the wall flow mode including the deposition of soot onto the porous filter walls, while the exhaust flows through them. On the other hand, the loaded DPF can cause a backpressure potentially decreasing the engine efficiency. Hence, a regeneration step at above 600 °C is mandatory to thermally remove the soot deposits from the filter, while the diesel exhaust gas is typically at 180–400 °C [4,5].

An alternative technique is using catalysts in two different ways: the addition of the catalyst to the fuel in form of organic derivatives of active metals and the deposition of a catalytic coating onto the filter surface. In this way, soot particles can combust at lower temperatures [6]. Noble metals [7], transition metal oxides [8], alkaline metal oxides [9], perovskite-like oxides [10] and rare earth oxides [11] are some of the catalysts which exhibited good catalytic performances. Transition metal oxides such as MnO_x [11], FeO_x [12], CoO_x [13] and CuO_x [14] have been used as the main catalysts for soot oxidation because of their redox catalytic cycles. Most of the oxide catalysts provide enough activities for soot oxidation only at temperatures higher than 400 °C. However, in recent years, some researchers have focused on the development of catalysts to lower the catalytic oxidation temperature of the diesel soot below 300 °C [15,16].

The role of transition metal catalysts in soot oxidation reaction is oxygen transfer from their surface to the soot [17]. Therefore, a critical issue affecting the performance of catalysts for soot oxidation is the contact condition between the catalyst and soot [18,19]. Three types of soot–catalyst contacts are examined in previous studies: (I) mixing soot and catalyst with just a spatula (loose contact), (II) mixing in a mechanical mill (tight contact), and (III) passing the diesel exhaust gas containing soot over a catalyst bed (in situ con-

* Corresponding author.
** Corresponding author. Fax: +98 21 66967793.
E-mail addresses: khodadad@ut.ac.ir (A.A. Khodadadi), mortazav@ut.ac.ir (Y. Mortazavi).

http://dx.doi.org/10.1016/j.apcatb.2015.09.019
0926-3373/

tact). It is reported that the results of "loose contact" and "in situ contact" are almost the same [20].

The non-thermal plasma (NTP) technology offers an innovative process for soot oxidation. In this method, the energy delivered to the system helps electrons to accelerate and gain a typical temperature of 10,000–250,000 K, while the background gas temperature does not rise significantly. The electrons collide with background molecules (N_2, O_2, and H_2O) and produce secondary electrons, photons, ions and radicals which accelerate the soot oxidation reaction [21,22]. The reaction of O atoms with carbon is estimated to be about 40 times higher than that of O_2 molecules [23]. Various types of discharges including corona [24], pulsed-corona [25] and dielectric barrier discharge [26] have been investigated. However, the process efficiency of NTP technology does not allow the achievement of both high conversion and CO_2 selectivity [27]. To overcome this limitation, an innovative technology of coupling the plasma reactor with a catalyst has been proposed.

Previous works indicate that the hybridization of NTP with a catalyst often causes a synergetic effect on the soot oxidation efficiency [28,29]. This synergetic effect can be explained by the short-living reactive species formed in the discharge [30]. It has been suggested that these species play an important role in promoting the re-oxidation of metal oxide vacancies generated in oxidation reaction in the discharge [31]. However, coupling mechanisms involved in this synergy have not been fully understood, and little information exists about the role of these reactive species [32]. Also, ozone is an important by-product in the plasma and is thermally stable up to 200 °C. Thermal and catalytic decomposition of ozone not only result in an increased energy efficiency, but also this harmful component is removed from the outlet gas stream [30].

In this work, the soot oxidation was investigated using a pin-to-plate corona plasma coupled with metal oxides in a catalytic reactor under diesel exhaust gas conditions. The effects of energy injection, temperature, and presence of NO_x and water vapor were also studied. The specific surface area, particle size, reducibility, and oxygen storage capacity of the metals (Mn, Co, and Fe) oxides are correlated with their soot oxidation activity.

2. Experimental

The catalyst samples, their characterization methods, and the plasma-(catalytic) soot oxidation variables investigated in in-situ and mostly tight contacts are summarized in Fig. 1.

2.1. Catalyst preparation

The metal oxides were synthesized by a precipitation method. Proper amounts of $Mn(NO_3)_2{\cdot}4H_2O$, $Co(NO_3)_2{\cdot}6H_2O$ and $Fe(NO_3)_3{\cdot}9H_2O$ (all from Merck) were dissolved in 250 ml of deionized water to obtain 0.5 M aqueous solutions. 1.0 M ammonia solution was added to the solutions drop wise at room temperature under vigorous stirring to adjust the pH value at about 10. The samples were kept under moderate stirring for 6 h [33], and then centrifuged to separate their solids. The solids were washed to neutrality with deionized water, dried at 80 °C for 12 h, and calcined at 400 °C in air for 3 h.

2.2. Catalysts and soot characterization

The specific surface areas (S_{BET}) of the catalysts and soot were determined at the liquid nitrogen temperature by the adsorption and desorption isotherms of nitrogen using a Quantachrome CHEMBET-3000 apparatus. Prior to BET and H_2-temperature programmed reduction (H_2-TPR) measurements, each sample was pretreated at 300 °C for 1 h in a flow of 10 sccm of nitrogen, to remove possible impurities, e.g. adsorbed H_2O. The average particle sizes were calculated from BET specific surface areas, assuming mono-dispersed spherical nanoparticles.

The surface morphology of the samples was determined by a scanning electron microscopy (SEM), using a Zeiss Sigma instrument. The catalysts uniform dispersion in the soot was measured by energy dispersive X-ray (EDX) elemental mapping.

X-ray diffraction (XRD) patterns of the catalysts were obtained by a Philips PW 1800 diffractometer using Cu-Kα radiation (40 kV/30 mA). The diffractograms were recorded from 2θ of 10–100° with a step-size $\Delta(2\theta)$ of 0.02° and a time of 0.35 s per step. The oxide phase analyses were done based on JCPDS files. The mean crystallite size of the catalysts was calculated using the Scherrer's equation (Eq. (1)).

$$d_{XRD} = \frac{k\lambda}{\beta \cos\theta} \quad (1)$$

where, k is a constant equal to 0.89, λ is the wavelength of the used X-ray equal to 0.15418 nm, β is the half-peak width and θ is the diffraction angle of main peak.

The H_2-TPR experiments of the samples were conducted in the CHEMBET-3000 apparatus. 10 sccm of 7% H_2 in Ar was passed through 25 mg of each sample, while the temperature was linearly increased at a rate of 10 °C/min to 1000 °C. The thermal conductivity detector (TCD) of the apparatus monitored the H_2 consumption in the TPR reactor. The TCD signal was calibrated by reduction of Ag_2O under the same conditions as the TPR test.

The O_2-temperature programmed desorption (O_2-TPD) of the catalysts was performed using the same apparatus as BET surface area measurement. Prior to each TPD run, 25 mg of each sample was pretreated at 300 °C for 1 h, and then cooled down to room temperature, in a flow of 10 sccm oxygen. This let the catalysts to be fully oxidized and adsorb oxygen on its surface. The catalyst was then exposed to a flow of 10 sccm He for 30 min at room temperature, to purge the reactor and clean the surface of catalyst from the weakly bonded oxygen. Finally, the sample was heated to 1000 °C at a rate of 10 °C/min under the same flow of helium and the desorbed oxygen was detected by the TCD.

The temperature programmed oxidation (TPO) of 7 mg catalyst in tight contact with 3.5 mg soot was also performed. The feed gas with a flow rate of 300 sccm consisting 10% O_2 in N_2 was controlled by two mass flow controllers. In all TPO runs, the temperature was increased to 600 °C at a rate of 10 °C/min. The effluent gases of each TPO run were analyzed by a Fourier-transform infrared spectrometer (FTIR, Bruker Vector 22).

2.3. Plasma-catalytic oxidation of soot

Fig. 2A shows the plasma-catalytic soot oxidation system including a pin-to-plate corona plasma reactor, a home-made DC power supply (0–20 kV), a gas supply manifold, and the analytical instrumentations. 300 sccm of the feed gas containing 10% O_2 in N_2, similar to the oxygen concentration in the diesel exhaust gas, was passed through the reactor. The air and N_2 gas flow rates, to obtain such a feed gas, were regulated by Unit mass flow controllers. To investigate the effects of 3.5% H_2O vapor on the soot oxidation performance, air was passed through a bubbler containing deionized water at room temperature. The reactor effluent gas was analyzed by the on-line FTIR equipped with a gas cell. The FTIR spectra were obtained with 4 cm^{-1} resolution every 30 s. A Carle 400-A gas chromatograph (GC) equipped with a methanizer comprising a Ru/Al_2O_3 catalyst at 420 °C was used for quantitative analysis of the reactor effluent gases. The inlet gas was also analyzed by bypassing the reactor feed directly into the FTIR and GC, using two 3-way valves. Based on the reactor volume and feed flow rate, the residence time in the plasma-catalytic reactor is 0.94 s.

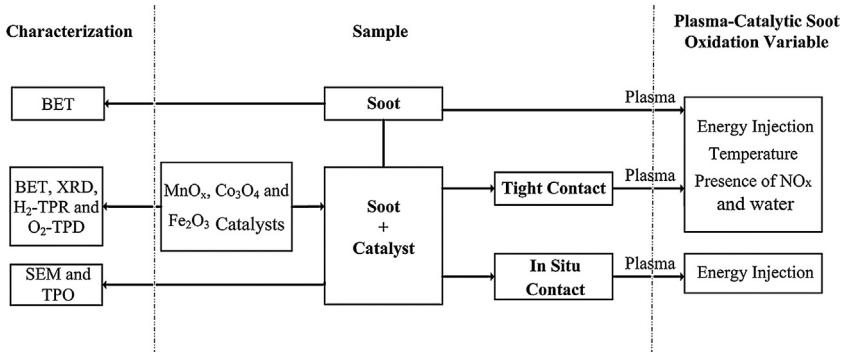

Fig. 1. A schematic diagram of soot and its combination with MnO_x, Co_3O_4 or Fe_2O_3 catalysts, their characterization and plasma-catalytic oxidation steps and variables.

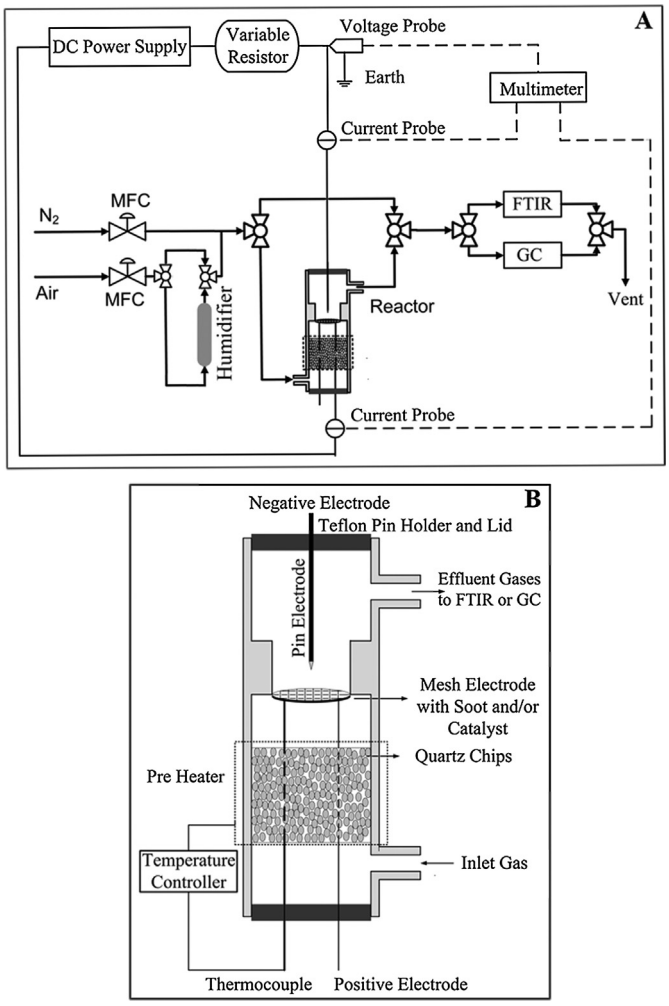

Fig. 2. (A) A schematic diagram of the experimental soot oxidation set-up and (B) the details of the pin-to-plate corona plasma reactor.

Fig. 2B illustrates the details of the pin-to-plate corona plasma reactor. It was comprised of a plate electrode of 10 mm diameter made of stainless steel mesh with 30 μm openings and one platinum pin electrode of 200 μm diameter. The cylindrical Pyrex reactor of 15 cm length and 16 mm ID, which reduces to 10 mm ID in the plasma zone, was used for the catalytic soot oxidation under plasma discharge conditions. The pin and plate electrodes with the discharge gap of 15 mm were connected to the negative and positive electrodes of a DC high voltage power supply, respectively. A K-type thermocouple was used beneath the plate electrode for monitoring and controlling the temperature of the plate electrode. The feed gas was passed through quartz chips column of 7 cm height to preheat the inlet gas to the specific temperature of the plasma-catalytic reaction.

The electrical discharge was ignited by applying a DC high voltage (0–20 kV) between the positive and negative electrodes of the reactor. The variable resistor (Fig. 2A) was set to an optimum value to form stable corona plasma without sparking. The voltage of the plasma discharge was measured by a high voltage probe (Pintek HVP-40, 1000:1) and the low voltage probe was used to measure the current from the voltage drop across a 100 Ω sampling resistor connected in series with the variable resistor. The analogue signals from the voltage and current probes were monitored with a digital multimeter (DT9205A). The energy injection (EI) rate in watt was calculated using Eq. (2).

$$\mathrm{EI} = V \times I \tag{2}$$

where V and I are the discharge voltage [V] and current [A], respectively.

Printex-U carbon black with S_{BET} and average particle size of 72 m^2/g and 25 nm was coated on the surface of the mesh electrode already polished and washed with acetone. The carbon black was selected because of its similar behavior to the laboratory-produced diesel soot [34]. To coat the electrode surface with 3.5 mg of the soot, 150 μl of a 23 mg/ml soot suspension in toluene was dropped on the mesh electrode and dried at 80 °C for 12 h. Two methods were employed to deposit 7 mg of a catalyst and 3.5 mg of the soot on the electrode. In the first method, 150 μl of a 46 mg/ml catalyst suspension in deionized water was deposited on the surface of the mesh electrode and was dried at 50 °C for 12 h. Then, the soot was deposited on the layer of the catalyst as explained previously and was heated at 100 °C for 2 h to obtain the in situ contact between soot and catalyst that is considered representative of the real contact between the soot and catalyst in a catalyzed soot filter [35]. In the second method, a mixed soot/catalyst suspension with a mass ratio of 1/2 in toluene was prepared by the means of ultrasonic. 300 μl of the suspension was dropped on the electrode, dried and heated at 100 °C for 2 h to get the tight contact.

The soot oxidation rate ($r_{oxidation}$ [mg/min]) was defined as follows:

$$r_{\mathrm{oxidation}} = \frac{PM_{(c)}}{RT} \times r_{\mathrm{CO+CO_2}} \tag{3}$$

where $M_{(c)}$ is the atomic weight of carbon [12 g/mol], P is the atmospheric pressure [1 atm], R is the gas constant [L atm/K mol], T is the temperature of FTIR analysis cell [K], and r_{CO+CO_2} is the generation rate of CO and CO_2 in the plasma reactor [ml/min]. The generation rate of CO and CO_2 (r_i [ml/min]) were calculated using Eq. (4).

$$r_i = F \times C_i \tag{4}$$

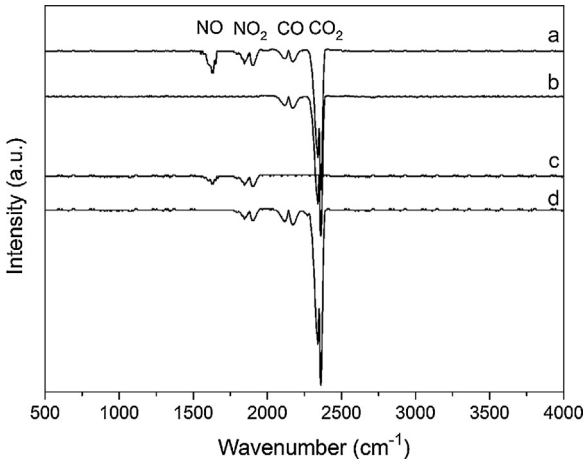

Fig. 3. FTIR spectra of outlet gas streams of the corona reactor in a N_2/O_2 flow of (a) 150 and (b) 300 sccm, (c) feed gas containing 450 ppm NO_x and (d) outlet gas in a 300 sccm $N_2/O_2/NO_x$.

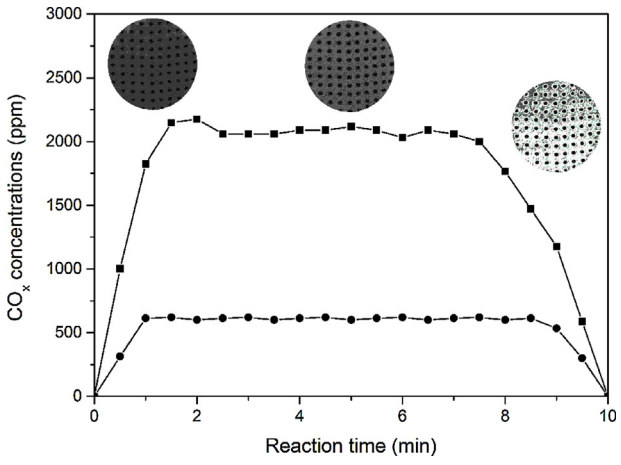

Fig. 4. The corona plasma reactor effluent concentrations of (●) CO and (■) CO_2 and the schematics of soot on the plate electrodes as a function of oxidation time, at 250°C and 7.4 W.

where F is the total gas flow rate [ml/min], and C_i is the molar concentration of each species in the effluent gas [ppm].

The soot removal efficiency (SRE) [g/kWh] on the basis of energy injection (EI) and CO_2 selectivity were defined as Eqs. (5) and (6).

$$\mathrm{SRE} = \frac{m \times 1000}{\mathrm{EI} \times t} \tag{5}$$

$$\mathrm{CO_2 selectivity} = \frac{C_{\mathrm{CO_2}}}{C_{\mathrm{CO_2}} + C_{\mathrm{CO}}} \tag{6}$$

where m is the amount of soot removed in the reaction [g], EI is the energy injection [W], t is the time for complete oxidation [h], and C_{CO} and C_{CO_2} are the molar concentrations of CO and CO_2 in the effluent gas [ppm].

3. Result and discussion

3.1. Corona plasma soot oxidation without using catalysts

Fig. 3 presents the FTIR spectra of the effluent gases from the pin-to-plate corona reactor at 250 °C and EI of 5.7 W, when the feed gas flow rate is 150 (a) and 300 sccm (b). The soot oxidation products are only CO and CO_2. Although there is no hazardous NO_x formation at the 300 sccm flow rate, significant amounts of NO and NO_2 are formed at 150 sccm. The EI of 5.7 W and a higher gas residence time for 150 sccm flow rate seem to be enough for breaking down N_2 molecules. The gas flow rate of 300 sccm was used for the rest of soot removal runs.

Fig. 4 shows CO and CO_2 concentration of the reactor effluent gases and the schematics of the plate (mesh) electrode including the soot at various reaction times during the soot oxidation at 250 °C and EI of 7.4 W. The CO_x concentrations in the effluent gas rise in the first minute, due to the mixing in the transfer lines to the FTIR and its gas cell. During 2–8 min of the reaction time, the concentrations of CO and CO_2 are nearly constant at 620 and 2100 ppm, respectively, while, the soot on the mesh electrode reduces, as shown in the inset schemes of Fig. 4. Then, the CO_x concentrations sharply decrease to zero and the soot on the plate electrode is completely oxidized. At 10 min of reaction time, the CO_x carbon balance is 96%, which indicates nearly total conversion of soot to CO and CO_2. It is concluded that the soot can be removed completely by corona plasma at 250 °C. However, the soot combustion ignition temperature in the absence of plasma is about 600 °C. Combustion at low temperatures is the main reason why plasma is used to remove diesel engine soot. The plasma discharge produces active oxygen species, and it dramatically lowers the soot oxidation temperature in the range of the diesel exhaust gas temperatures of 180–350 °C [36].

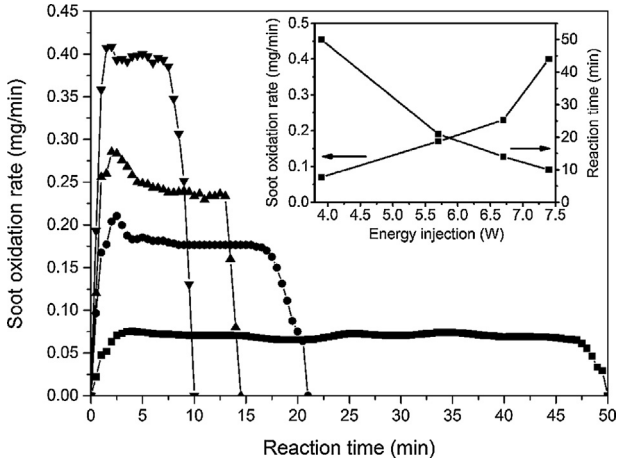

Fig. 5. Soot oxidation rates at energy injections of (■) 3.9 W, (●) 5.7 W, (▲) 6.7 W and (▼) 7.4 W during the reaction time in the corona plasma reactor without catalyst at 250 °C. The inset shows the soot oxidation rate and its complete oxidation time as a function of energy injection.

3.1.1. Energy injection effects

Fig. 5 shows the soot oxidation rates as a function of reaction time at 250 °C and various EIs in the range of 3.9–7.4 W adjusted by changing the voltage. The overshoots in the oxidation rates at EIs of 5.7 and 6.7 W may be due to the change in the distribution of soot on the mesh plate electrode. The Fig. 5 inset indicates the time of total oxidation and the oxidation rate at the plateau region as a function of EI. When EI increases from 3.9 to 7.4 W, the soot oxidation rates enhance by 5.7 times from 0.07 to 0.40 mg/min and the oxidation times decrease 5.0 times from 50 to 10 min. It is suggested that reactive oxygen species generated within the discharge play an important role in the soot oxidation [36]. The higher energy injection produces more reactive species, accelerates the soot oxidation, and depletes the soot more rapidly [37].

3.1.2. Gas temperature effects

Fig. 6A and B indicates the soot removal efficiency (SRE) and CO_2 selectivity as a function of EI at various gas temperatures in the range of 180–350 °C, corresponding to the diesel exhaust gas

Table 1
The reported results of soot removal for different kinds of plasma reactors.

Plasma type	Carbonaceous particulate matter (PM)	Maximum energy efficiency (g/KWh)	Energy injection (W)	References
DBD[a]	PM	2.90	345	[23]
DBD	PM	1.70	180	[40]
Wire to cylinder	PM	2.20	17.2	[41]
Corona	Activated carbon	8.18	23	[42]
Corona	Soot	5.04	7.4	This study

[a] Dielectric barrier discharge

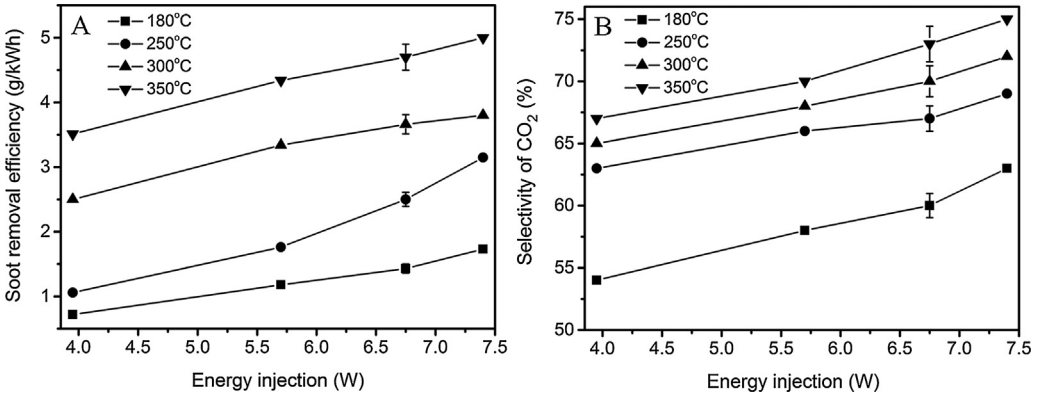

Fig. 6. (A) Soot removal efficiency and (B) CO_2 selectivity as a function of energy injection at various gas temperatures using the corona plasma reactor without catalyst.

temperatures. The SRE and selectivity of CO_2 increase significantly with both gas temperature and EI. At an EI of 3.9 W, SRE increases from 0.73 to 3.50 g/kWh, when the temperature increases from 180 to 350 °C. At 5.7 W, a sharp increase in SRE is observed, when the temperature increases from 250 to 350 °C. The soot removal efficiency reaches its highest value of 5.04 g/kWh at 350 °C and 7.4 W. The concentration of CO_2 is higher than CO at all EIs and gas temperatures. The relative standard deviations (RSD) of SRE and CO_2 selectivity are about 4% and 3%, respectively.

Ozone formed in the plasma reactor is thermally decomposed to O_2 and O radicals at temperatures higher than 200 °C. The O radicals play important roles in the oxidation reaction. The increase in the ozone decomposition rate with temperature as well as interactions between reactive oxygen atoms and soot particles are the reasons why SRE increases with temperature [38,39]. The higher rate of ozone decomposition to O radicals at higher temperatures and EIs not only facilitates the soot oxidation but also accelerates CO oxidation to CO_2.

Table 1 summarizes energy injections (EIs) and efficiencies of soot oxidation in different kinds of plasmas, reported in the literature. Compared to others works, this study shows higher or comparable energy efficiencies at much lower energy injections (EIs).

3.2. Catalyst characterization

XRD patterns of the calcined manganese, iron and cobalt oxide catalysts are illustrated in Fig. 7. The diffraction lines of the manganese oxide (Fig. 7a) indicate a mixture of Mn_3O_4 with an orthorhombic structure referenced in the JCPDS 16-0350 file and Mn_2O_3 with a tetragonal structure referenced in the JCPDS 06-0540 file. The peaks at 2θ of 29°, 32°, 36°, 49° and 58° are overlapping peaks for both Mn_2O_3 and Mn_3O_4. The peaks at 2θ of 18° and 60° correspond to Mn_2O_3 and diffraction peaks at 2θ of 38°, 39° and 48° are attributed to Mn_3O_4 structure. The diffraction profile of the iron oxide (Fig. 7b) corresponds to Fe_2O_3 with a rhombohedral structure

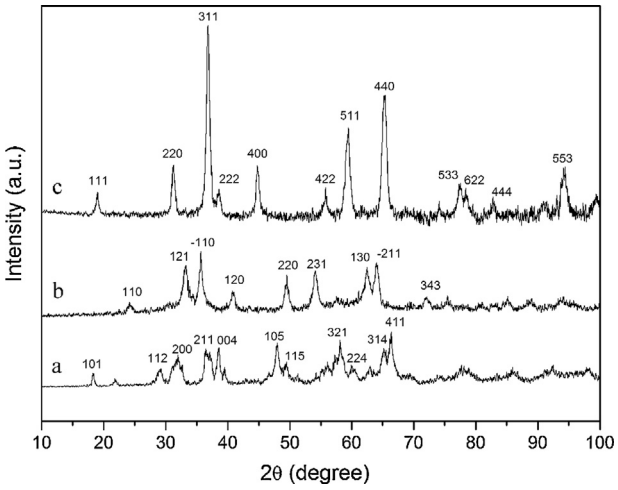

Fig. 7. XRD patterns of (a) manganese oxide, (b) iron oxide and (c) cobalt oxide samples.

as referenced in the JCPDS 01-073-2234 file. The diffraction lines of the cobalt oxide (Fig. 7c) match the JCPDS 9-0418 file identifying Co_3O_4 with a cubic structure. The mean crystallite sizes of the catalysts are calculated from XRD patterns by Scherrer's method using the peaks at 2θ of 36°, 33° and 37° for MnO_x, Fe_2O_3 and Co_3O_4, respectively, and are presented in Table 2. All catalysts are composed of nano-sized crystallites.

BET surface area and average particle size of MnO_x, Co_3O_4 and Fe_2O_3 samples are presented in Table 2. Fe_2O_3 has the highest specific surface area of 137.8 m^2/g, which is compatible with its low average crystallite size.

SEM images of the mixtures of soot and either Fe_2O_3, Co_3O_4 or MnO_x nanoparticles are illustrated in Fig. 8A–C, respectively. SEM images show large agglomerates with spherical shape and large pores. The porous structure facilitates diffusion of oxygen species to

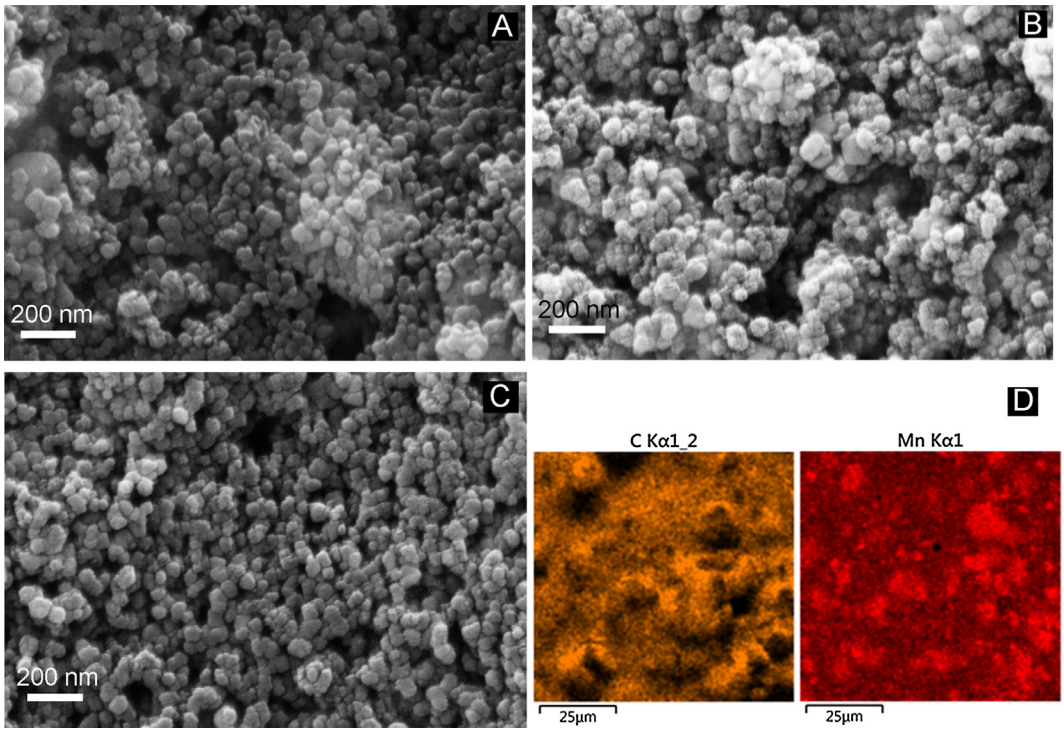

Fig. 8. SEM images of mixtures of soot and (A) Fe_2O_3, (B) Co_3O_4 and (C) MnO_x nanoparticles and (D) dot-mapping images of MnO_x nanoparticles and soot particles.

Table 2
BET surface areas, particle and crystallite sizes of the catalysts and the relative quantities of oxygen released by each catalyst at different temperatures related to the plasma-catalytic soot oxidation temperatures.

Samples	MnO_x	Co_3O_4	Fe_2O_3
S_{BET} (m^2/g)	22.3	61.3	137.8
d_{BET} (nm)	55.4	16.0	8.3
d_{XRD} (nm)	168.1	53.3	14.6
Des1	9	41	107
Des2	55	43	201
Des3	263	45	295
Des4	1648	52	570

Des: The O_2 desorption peak area in the ranges of (1) 0–180, (2) 0–250, (3) 0–300 and (4) 0–350 °C.

the surface of soot particles. The EDX dot-mapping images of MnO_x nanoparticles and soot display a micron-scale uniform distribution of manganese oxide and soot (carbonaceous) particles throughout the powder (Fig. 8D). The uniform distribution implies the high number of contact points of the catalyst and soot for acceleration of oxygen transfer from the catalyst to soot [43].

The reducibility of the catalysts measured by H_2-TPR experiments is shown in Fig. 9. Fig. 9a illustrates the deconvoluted H_2-TPR profile of MnO_x, which includes two reduction peaks. Deconvolution of the H_2-TPR peaks allows calculating the amount of H_2 uptake in each peak. The first peak in the temperature range of 150–350 °C with 3743 μmol H_2 consumed/g can be ascribed to the reduction of Mn_2O_3 according to Eq. (7). The second peak at 350–550 °C with consumption of 4674 μmol H_2/g may be attributed to the reduction of Mn_3O_4 to MnO according to Eq. (8) [43].

$$3Mn_2O_3 + H_2 \rightarrow 2Mn_3O_4 + H_2O \quad (7)$$

$$Mn_3O_4 + H_2 \rightarrow 3MnO + H_2O \quad (8)$$

Fig. 9b shows the deconvoluted H_2–TPR profile of Co_3O_4 with three reduction peaks at 100–230, 230–360 and 360–500 °C. The first peak corresponds to the reduction of surface oxygen species [44]. The second peak with 1754 μmol H_2/g consumption is associated with the reduction of Co^{3+} ions to Co^{2+} (Eq. (9)), while the last peak with 5869 μmol H_2/g is ascribed to the reduction of the CoO to metallic cobalt (Eq. (10)) [45].

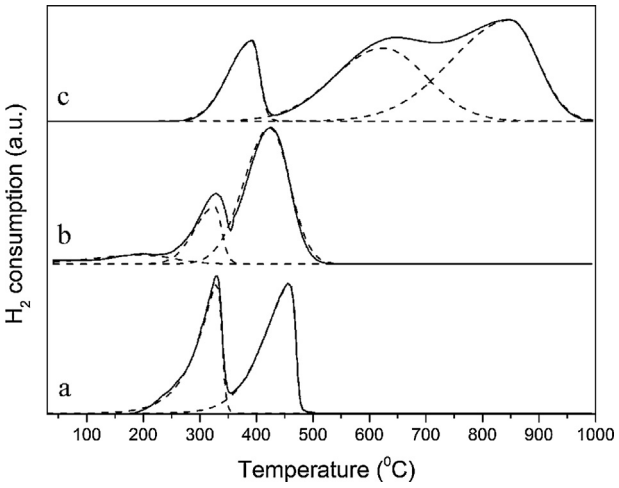

Fig. 9. The H_2-TPR profiles of (a) manganese oxide, (b) cobalt oxide and (c) iron oxide catalysts.

$$Co_3O_4 + H_2 \rightarrow 3CoO + H_2O \quad (9)$$

$$3CoO + 3H_2 \rightarrow 3Co + 3H_2O \quad (10)$$

The H_2–TPR profile of Fe_2O_3 (Fig. 9c) shows three peaks at the temperature ranges of 250–430, 430–724 and 724–1000 °C. The first peak with H_2 consumption quantity of 2413 μmol/g corresponds to the reduction of Fe_2O_3 to Fe_3O_4 (Eq. (11)). The second and third peaks with H_2 consumption quantities of 6676 and 8673 μmol/g can be related to the reduction of Fe_3O_4 and FeO (Eqs. (12) and (13)), respectively [46].

$$3Fe_2O_3 + H_2 \rightarrow 2Fe_3O_4 + H_2O \quad (11)$$

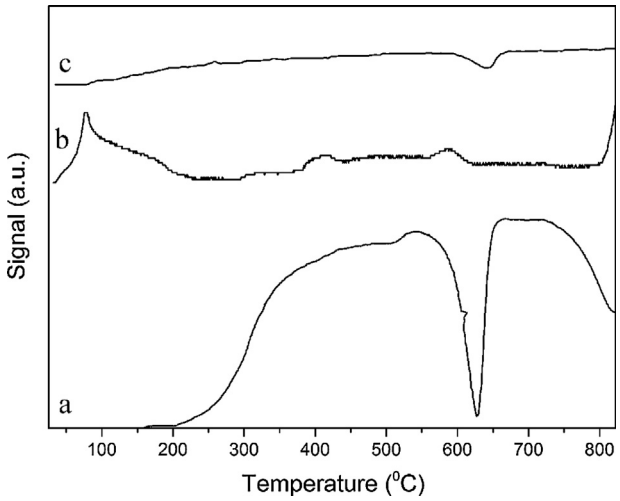

Fig. 10. The O_2-TPD profiles of the (a) manganese oxide, (b) cobalt oxide and (c) iron oxide catalysts.

$$2Fe_3O_4 + 2H_2 \rightarrow 6FeO + 2H_2O \quad (12)$$

$$6FeO + 6H_2 \rightarrow 6Fe + 6H_2O \quad (13)$$

The contributions of the thermal oxygen release from various catalysts were investigated by O_2-TPD experiments, the profiles of which are presented in Fig. 10. The O_2-TPD profile of MnO_x (Fig. 10a) shows two ranges of desorption peaks: (1) the largest peak in the temperature range of 200–630 °C attributed to α-oxygen, and (2) the other one in the temperature range of 630–820 °C related to β-oxygen [47]. The first peak is referred to the adsorbed oxygen bound to the vacancies of surface anions and is more mobile. The latter peak is attributed to the more strongly bound oxygen species [48]. The O_2-TPD profile of Co_3O_4 is shown in Fig. 10b. The profile includes two ranges of oxygen desorption. The low temperature peak is observed between 40 and 220 °C and is attributed to α-oxygen (surface oxygen), while the larger peak at the temperature range of 780–920 °C not shown in Fig. 10 is ascribed to β-oxygen (bulk oxygen) [47]. Fig. 10c indicates O_2-TPD profile of Fe_2O_3. Two oxygen desorption peaks at 100–640 and 640–1000 °C can be assigned to suprafacial oxygen and interfacial one not fully developed at 950 °C [47].

Table 2 presents the O_2 desorption peak areas of the catalyst samples at different temperatures corresponding to the plasma-catalytic oxidation temperatures. This is related to the quantities of oxygen possibly released by each catalyst at the soot oxidation temperatures. Complete soot oxidation strongly depends on the oxygen adsorption capacity of the metal oxide catalysts [43]. The considerable amounts of oxygen adsorbed on the surface of MnO_x and Fe_2O_3 cause the complete oxidation of soot.

The soot oxidation activity of the catalysts, in the absence of plasma discharge, was investigated by TPO of a mixture of the soot and each catalyst. Fig. 11 shows the TPO profiles of the mixtures of soot and either Fe_2O_3, MnO_x or Co_3O_4 catalyst. In all of the TPO tests, the soot is completely oxidized at temperatures lower than 600 °C, as inferred from CO_2 formation. No significant amount of soot is oxidized at temperatures lower than 350 °C, which corresponds to the maximum temperature of the diesel exhaust used for plasma-catalytic oxidation of soot. The CO_2 peaks temperatures are 425, 454 and 470 °C for the mixtures of soot and either MnO_x, Fe_2O_3 or Co_3O_4 catalysts, respectively. MnO_x shows the highest oxygen storage capacity and reducibility at about 350 °C, based on the highest amount of H_2 uptake (3743 μmol H_2/g) and O_2 desorption peak area (1648) determined by H_2-TPR and O_2-TPD tests, respectively. In accordance with H_2-TPR and O_2-TPD results, MnO_x presents the lowest soot oxidation peak temperature of 425 °C in the TPO test.

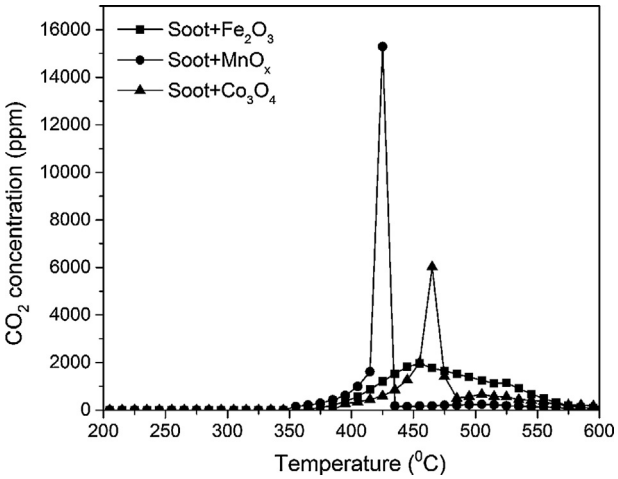

Fig. 11. The TPO profiles of the mixture of soot and catalysts.

3.3. Plasma-catalytic soot oxidation

The effects of MnO_x, Co_3O_4 and Fe_2O_3 metal oxides on the soot oxidation were investigated in the corona plasma reactor at various gas temperatures and energy injections (EIs) in this section. The effects of soot–catalyst contact type and the presence of NO_x and H_2O were also studied.

3.3.1. Soot–catalyst contact type

Fig. 12A and B presents soot removal efficiency (SRE) and selectivity of CO_2, respectively, as a function of gas temperature at an EI of 5.7 W, using MnO_x catalyst in the in-situ and tight contacts with soot. SRE and CO_2 selectivity significantly increase with the gas temperature for both contact types. Also, tight contact shows up to 44 and 17% higher SRE and selectivity, respectively. The significant difference in the performance of in-situ and tight contacts is typical for solid–solid reactions. It is reported that the role of catalysts in soot oxidation lies in the transfer of oxygen to soot through physical contact points [12]. The mechanism of the catalytic soot oxidation depends on the proximity of catalyst and soot [49]. In the tight contact, there are greater numbers of contact points between the soot and catalyst, resulting in the higher soot removal efficiency.

To evaluate the reusability of the catalyst, used MnO_x was collected after soot complete oxidation and mixed with soot again and coated on the surface of the mesh electrode for the soot oxidation. The used MnO_x shows 64% of its initial activity.

3.3.2. Plasma-catalytic soot oxidation on different metal oxides

Fig. 13A and B shows SRE and CO_2 selectivity at different temperatures and EIs of 3.9 and 7.4 W in the absence and presence of Fe_2O_3, MnO_x and Co_3O_4 catalysts in tight contact with the soot, respectively. The SRE and CO_2 selectivity in the presence of the catalysts, like in their absence, dramatically increase with temperature and energy injection (EI). In addition, SRE and CO_2 selectivity significantly enhance, when the catalysts are used in the corona reactor. At 3.9 W, maximum SRE and CO_2 selectivity enhancements of 77 and 29% are observed, respectively, when MnO_x catalyst is used at the high temperature of 350 °C. However, the SRE enhancement of 40% is observed at 3.9 W, when Fe_2O_3 catalyst is used at the low temperature of 180 °C. The SRE and selectivity enhancements are in the order of Fe > Co > Mn and Mn > Fe > Co oxides catalysts at the low temperatures of 180 and 250 °C and high temperatures of 300 and 350 °C, respectively. Increasing CO_2 selectivity in the presence

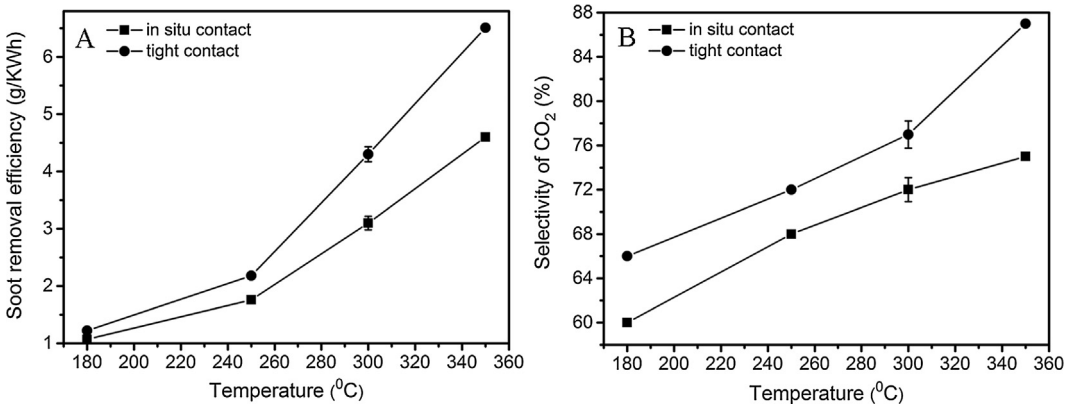

Fig. 12. (A) Energy efficiency of soot removal and (B) selectivity of CO_2 using the corona reactor with MnO_x catalyst at various gas temperatures and 5.7 W with two contact types.

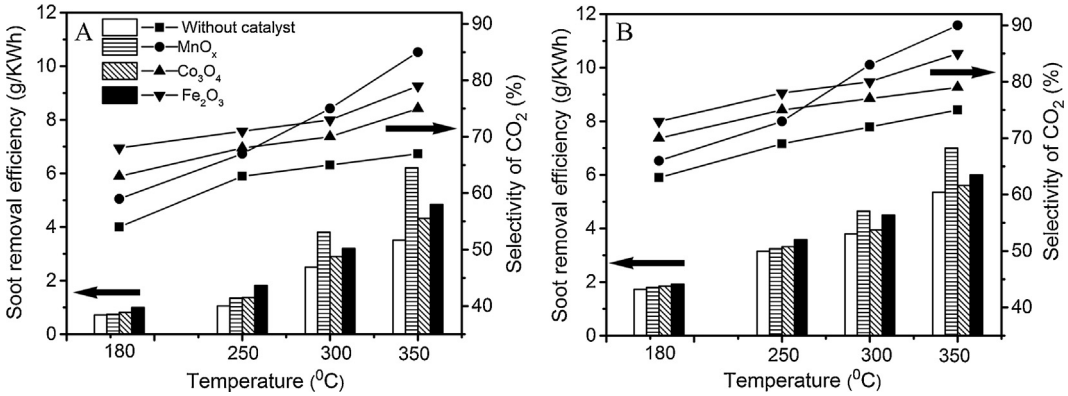

Fig. 13. Soot removal efficiency and selectivity of CO_2 as a function of temperature in the absence and presence of Fe_2O_3, MnO_x and Co_3O_4 catalyst at EIs of (A) 3.9 and (B) 7.4 W.

of the catalysts is referred to their CO oxidation activity, which may be related to the accelerated oxygen transfer from the catalysts [50]. Maximum values of soot removal efficiency (SRE) in the presence of Fe_2O_3, MnO_x and Co_3O_4 catalysts are 6.0, 7.0 and 5.6 g/kWh, respectively, at 350 °C and 7.4 W. Also, CO_2 selectivity in the presence of Fe_2O_3, MnO_x and Co_3O_4 reaches to the maximum values of 85, 90 and 79%, respectively, at 350 °C and 7.4 W.

The activated oxygen from the catalyst surface can oxidize soot particulates and CO and then the reduced catalyst is re-oxidized by plasma discharge products such as O and O_3 [51]. As a result, the catalyst with a high O_2 storage capacity and reducibility has higher activity toward soot and CO oxidation. Another important factor for high catalytic activity in soot oxidation reaction is external surface area of catalysts. The outer surface area of catalyst can provide the necessary active sites for catalytic reactions. The catalyst with smaller particle diameters has larger numbers of surface sites so the catalyst may have higher activity [18]. In addition, catalyst with high external surface area can easily transfer adsorbed oxygen to the soot particles via physical contact points [12]. On the other hand, the contact between the catalyst and soot is not at nanoscale, but the micron-size particles of the catalyst and soot are contacted as shown in Fig. 8D. However, the BET surface area shows the surface area between the nanoscale particles of the catalyst. Therefore, the oxygen mobility determined by O_2-TPD and H_2-TPR is the most effective parameter in the soot oxidation.

The increase in the soot and CO oxidation activity of the catalysts with the temperature may be correlated to the change of their reducibility and oxygen storage capacity with temperature measured by H_2-TPR and O_2-TPD (Figs. 9 and 10), respectively. Higher oxygen storage capacity and reducibility of MnO_x, as compared to Fe_2O_3 and Co_3O_4, at 300 and 350 °C may explain its high SRE and CO_2 selectivity. On the other hand, at the low temperatures of 180 and 250 °C, the soot and CO oxidation rate of Fe_2O_3 is higher than those of the MnO_x and Co_3O_4, due possibly to its higher surface area and oxygen storage capacity at the low temperatures.

Ozone plays an important role in the plasma catalytic processes. During the plasma-catalytic soot oxidation, besides the direct reaction of ozone with soot, its catalytic and thermal decomposition leads to the formation of reactive atomic oxygen on the surface of catalyst and in the gas phase. The oxygen atoms are very strong oxidants [52]. It is reported that the ozone decomposition on MnO_x occurs through an electron transfer from Mn^{n+} to an ozone molecule producing atomic oxygen on the surface of the catalyst which facilitates the refilling of metal oxide vacancies. Similar mechanisms are observed for other metal oxides [53].

In order to investigate the role of ozone and atomic oxygen, the ozone concentration in the outlet stream of plasma reactor was measured by FTIR in the presence of catalysts at 25, 180 and 250 °C. As the concentration of ozone produced in the corona reactor is less than the FTIR detection limit, ozone was concentrated in the reactor to be detectable by FTIR. The results show that ozone decomposition at room temperature in the presence of MnO_x, Fe_2O_3 and Co_3O_4 catalysts are 33.3, 20.1 and 17.2% under the plasma discharge condition, respectively. However, the conversion increases to 100% at temperatures above 180 °C for all catalysts. Therefore, the thermal and catalytic decomposition of ozone at temperatures above 180 °C causes the formation of reactive oxygen. Catalytic and thermal decomposition of ozone also result in the removal of this harmful component from the effluent gases.

Table 3
The synergy factor of SRE in the presence of each Fe_2O_3, MnO_x and Co_3O_4 catalyst at different temperatures and EIs of 3.9 and 7.4 W.

Temp (°C)	MnO_x		Co_3O_4		Fe_2O_3	
	3.9 W	7.4 W	3.9 W	7.4 W	3.9 W	7.4 W
180	1.04	1.04	1.14	1.07	1.39	1.11
250	1.27	1.03	1.29	1.05	1.72	1.14
300	1.52	1.22	1.16	1.04	1.28	1.18
350	1.77	1.31	1.23	1.05	1.38	1.12

Table 4
The synergy factor of CO_2 selectivity in the presence of each Fe_2O_3, MnO_x and Co_3O_4 catalyst at different temperatures and EIs.

Temp (°C)	MnO_x		Co_3O_4		Fe_2O_3	
	3.9 W	7.4 W	3.9 W	7.4 W	3.9 W	7.4 W
180	1.09	1.05	1.17	1.11	1.26	1.16
250	1.06	1.06	1.08	1.08	1.13	1.13
300	1.15	1.15	1.08	1.07	1.12	1.11
350	1.27	1.20	1.12	1.05	1.18	1.13

Metal oxides have synergetic effects on the soot oxidation promotion under plasma conditions. Refilling the metal oxides oxygen vacancies with O atoms produced in plasma discharge is the main reason for synergetic effect [31]. In order to investigate the synergy in this process, the synergy factor for SRE and CO_2 selectivity are defined as follow [54]:

$$f_{SRE} = \frac{SRE_{plasma-catalyst}}{SRE_{plasma} + SRE_{catalyst}} \quad (14)$$

$$f_{CO_2} = \frac{(selectivity_{CO_2})_{plasma-catalyst}}{(selectivity_{CO_2})_{plasma} + (selectivity_{CO_2})_{catalyst}} \quad (15)$$

TPO profiles of the mixtures of soot and catalysts (Fig. 11) show that the thermal catalytic soot oxidation rate is negligible at temperatures below 350 °C, so SRE and CO_2 selectivity in the presence of catalysts alone are negligible in comparison to their corresponding values in the plasma. The synergetic effect is observed, when the value of the synergy factor exceeds 1. Tables 3 and 4 show the synergy factors of SRE and CO_2 selectivity, respectively, in the presence of each Fe_2O_3, MnO_x and Co_3O_4 catalyst at different temperatures and EIs of 3.9 and 7.4 W. MnO_x and Fe_2O_3 have the highest synergetic effect at the high temperatures of 300 and 350 °C and low temperatures of 180 and 250 °C, respectively. The synergy factors of SRE and CO_2 selectivity are in the ranges of 1.03–1.77 and 1.05–1.27, respectively. As a result, the plasma-catalytic system shows a higher synergy with respect to SRE than to selectivity. Furthermore, the synergy factors decrease with EI, indicating that reactive species control the plasma-catalytic process at higher EIs and the role of catalyst decreases.

3.3.3. The effects of NO_x and H_2O vapor on the plasma-catalytic soot oxidation

Diesel engine exhaust gas inevitably contains approximately 450 ppm nitrogen oxides (NO_x) and 3.5% H_2O, which affect the soot oxidation [17,55]. Fig. 3 presents the FTIR spectra of the feed gas containing 450 ppm NO_x (c) and the effluent gas from the corona reactor in the presence of NO_x at 5.7 W (d). NO as the main hazardous gas in the diesel exhaust is completely removed in the plasma discharge, but NO_2 has slightly increased. Increase in NO_2 concentration is due to the oxidation of a portion of NO in the presence of O radicals and O_3 molecules [56]. Fig. 14 indicates SRE in the absence and presence of NO_x or H_2O in the corona plasma (-catalytic) reactor at an EI of 5.7 W and 300 °C. When NO_x is added to the feed gas, SRE increases by 10.0, 17.4, 11.4 and 11.2% in the absence and presence of MnO_x, Co_3O_4 and Fe_2O_3 catalysts, respectively. NO, NO_2 and the reactive species generated in the discharge facilitate the soot oxidation [37]. The catalysts with higher oxygen storage capacity tends to be re-oxidized more easily by oxidants such as O, NO and NO_2. As a result, NO and NO_2 molecules are broken down more easily in the presence of catalysts with higher oxygen storage capacities.

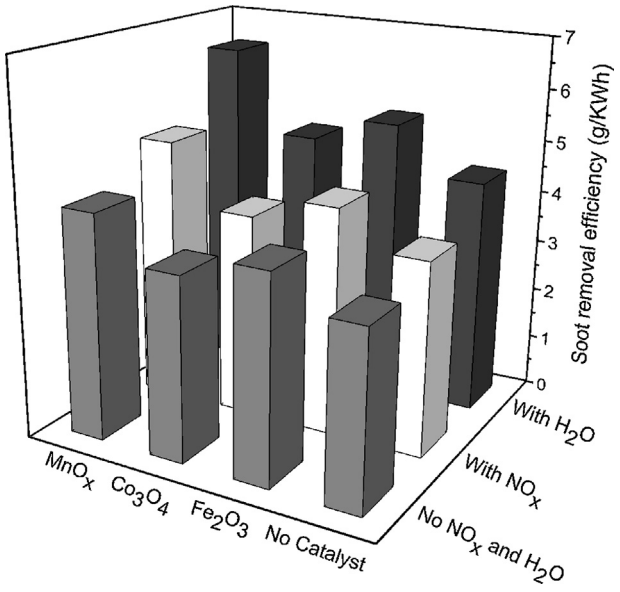

Fig. 14. The effect of 450 ppm NO_x and 3.5% H_2O in the feed gas on the energy efficiency of soot removal in the absence and presence of Co_3O_4, MnO_x and Fe_2O_3 catalysts at an EI of 5.7 W and 300 °C.

Enhancements of 34.1, 49.3, 39.2 and 37.0% in SREs are obtained in the absence and presence of MnO_x, Co_3O_4 and Fe_2O_3 catalysts, respectively, when 3.5% H_2O vapor is added to the feed gas. It is suggested that OH radicals generated from O atoms and H_2O molecules in the discharge play an important role in the soot oxidation. The enhancement by OH depends on the type of catalyst [57]. The OH radicals also facilitate the re-oxidization of the metal oxide vacancies generated by the consumption of oxygen. OH enhancement reaches the maximum value in the presence of MnO_x with the highest oxygen storage capacity.

3.4. Mechanism of plasma (-catalytic) soot oxidation

When a high voltage is applied in a gas, the gas molecules can be dissociated and/or ionized by the impact of electrons energized in the electric field with the gas molecules or atoms [36]. The plasma reactor parameters are optimized not to activate N_2 resulting in NO_x formation (Fig. 3). The following mechanism is proposed for soot oxidation by plasma discharge without catalyst [37,57].

Oxygen reactive species are generated in plasma discharge (Eq. (16)). Oxygen atoms combine with oxygen and H_2O molecules to generate ozone and OH radicals, respectively (Eqs. (17) and (18)). Soot oxidation at low temperatures may be attributed to reactive OH radicals, ozone (O_3) and O atoms generated in the corona discharge [55]. When CO and CO_2 are the only products, the oxidation reactions can be represented by Eqs. (19)–(21). Carbon dioxide is also produced by combination of carbon monoxide and oxygen (Eq. (22)).

$$O_2 + \vec{e} \rightarrow O + O + e \quad (16)$$

$$O + O_2 \leftrightarrow O_3 \quad (17)$$

$$O + H_2O \rightarrow 2OH \quad (18)$$

$$2C + 3O \rightarrow CO + CO_2 \quad (19)$$

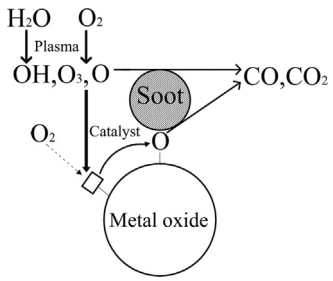

Fig. 15. Schematic mechanism of plasma-catalytic soot oxidation over a metal oxide.

$$2C + O_3 \rightarrow CO + CO_2 \quad (20)$$

$$2C + 3OH \rightarrow CO + CO_2 + 3H \quad (21)$$

$$CO + O \rightarrow CO_2 \quad (22)$$

where $\vec{e}$ denotes the energized electron.

Fig. 15 shows a mechanism for the soot oxidation in the plasma discharge over a metal oxide. Besides oxidation via O atoms, OH radicals and O_3 molecules, soot oxidation is promoted by the transfer of oxygen on the surface of active metal oxides sites (M) to the soot via soot–catalyst contact points (Eq. (23)) [12]. The metal oxides in this reaction act as a source of activated oxygen, which can be regenerated [20]. The release of oxygen leads to form partially reduced metal oxide sites denoted as M(*). These metal oxide vacancies can be refilled by oxidants present in the atmosphere (Eq. (24)). In the plasma discharge, additional refilling reactions are considered via O_3 molecules, O atoms and OH radicals generated by plasma discharge (Eqs. (25)–(27)). The dominating mechanism for refilling of the surface oxygen vacancy may be via reactive species generated by the plasma discharge as active oxidants. This is the main reason for the synergetic effect of plasma and catalyst [51]. Also, CO oxidation to CO_2 occurs by oxygen atoms on the surface of the metal oxides (Eq. (28)).

$$2C + 3M(O) \rightarrow CO + CO_2 + 3M(*) \quad (23)$$

$$O_2(g) + 2M(*) \rightarrow 2M(O) \quad (24)$$

$$O(g) + M(*) \rightarrow M(O) \quad (25)$$

$$O_3(g) + M(*) \rightarrow M(O) + O_2(g) \quad (26)$$

$$OH + M(*) \rightarrow M(O) + H \quad (27)$$

$$CO + M(O) \rightarrow CO_2 + M(*) \quad (28)$$

The following mechanism is also proposed for soot oxidation in Air/NO_x atmosphere in the plasma discharge. As shown in Section 3.3.3, NO_x is able to oxidize soot, the reactions of which are presented in Eqs. (29) and (30).

$$C + 2NO \rightarrow CO_2 + N_2 \quad (29)$$

$$C + NO_2 \rightarrow CO + NO \quad (30)$$

The species generated in the plasma also oxidize NO to NO_2 (Eqs. (31) and (32)) [58].

$$NO + O \rightarrow NO_2 \quad (31)$$

$$NO + O_3 \rightarrow NO_2 + O_2 \quad (32)$$

NO_x molecules as strong oxidants can refill the surface vacancies of metal oxides and provide sites for further oxidation reactions (Eqs. (33) and (34)).

$$2M(*) + 2NO \rightarrow 2M(O) + N_2 \quad (33)$$

$$M(*) + NO_2 \rightarrow M(O) + NO \quad (34)$$

4. Conclusion

Diesel soot and its mixture with various metal oxide catalysts were oxidized to CO and CO_2 in a corona plasma reactor under diesel exhaust gas conditions. The soot removal efficiency (SRE) and CO_2 selectivity increase with energy injection (EI), gas temperature, and the presence of NO_x and water vapor. A very high soot removal efficiency of 5.04 g/kWh is obtained at a low EI of 7.4 W. Although thermal catalytic soot oxidation rate is negligible at temperatures lower than 350 °C, SRE and CO_2 selectivity enhance up to 77 and 29%, respectively, when the catalyst is mixed with the soot in the plasma reactor. The best catalysts are MnO_x and Fe_2O_3 at the high and low temperatures, respectively. The soot oxidation activity of the metal oxides which act as regenerative sources of activated oxygen is correlated with the oxides oxygen storage capacities, reducibility and particle sizes. Oxygen supply to the soot seems to occur by reactive species generated in the plasma such as O atoms, OH radicals and O_3 molecules and the catalyst through its contact points with soot. In addition, the metal oxides oxygen vacancies generated by oxidation of soot are refilled more easily with the reactive species than with molecular oxygen. This explains the synergistic effects of metal oxides on the soot oxidation promotion under plasma conditions.

References

[1] A. Bueno-López, Appl. Catal. B 146 (2014) 1–11.
[2] K. Krishna, A. Bueno-Lopez, M. Makkee, J.A. Moulijn, Appl. Catal. B 75 (2007) 189–200.
[3] J. Oi-Uchisawa, S. Wang, T. Nanba, A. Ohi, A. Obuchi, Appl. Catal. B 44 (2003) 207–215.
[4] J. Liu, Z. Zhao, J. Lan, C. Xu, A. Duan, G. Jiang, X. Wang, H. He, J. Phys. Chem. C 113 (2009) 17114–17123.
[5] J. Zokoe, P.J. McGinn, Chem. Eng. J. 262 (2015) 68–77.
[6] D. Fino, V. Specchia, Powder Technol. 180 (2008) 64–73.
[7] A. Setiabudi, B.A.A.L.v. Setten, M. Makkee, J.A. Moulijn, Appl. Catal. B 35 (2002) 159–166.
[8] D. Reichert, T. Finke, N. Atanassova, H. Bockhorn, S. Kureti, Appl. Catal. B 84 (2008) 803.
[9] M. Sun, L. Wang, B. Feng, Z. Zhang, G. Lu, Y. Guo, Catal. Today 175 (2011) 100–105.
[10] J.L. Hueso, A. Caballero, M. Ocaña, A.R. González-Elipe, J. Catal. 257 (2008) 334–344.
[11] I. Atribak, A. Bueno-Lopez, A. Garcıa-Garcıa, P. Navarro, D. Frıas, M. Montes, Appl. Catal. B 93 (2010) 267–273.
[12] S. Wagloehner, S. Kureti, Appl. Catal. B 125 (2012) 158–165.
[13] J. Liu, Z. Zhao, J. Wang, C. Xu, A. Duan, G. Jiang, Q. Yang, Appl. Catal. B 84 (2008) 185–195.
[14] F.E. Lopez-Suarez, A. Bueno-Lopez, M.J. Illan-Gomez, Appl. Catal. B 84 (2008) 651–658.
[15] G. Corro, U. Pal, E. Ayala, E. Vidal, Catal. Today 212 (2013) 63–69.
[16] G. Corro, S. Cebada, U. Pal, J.L.G. Fierro, J. Alvarado, Appl. Catal. B 165 (2015) 555–565.
[17] N. Zouaoui, M. Issa, D. Kehrli, M. Jeguirim, Catal. Today 189 (2012) 65–69.
[18] J. Liu, Z. Zhao, C. Xu, A. Duan, J. Guiyuan, J. Rare Earths 28 (2010) 198–204.
[19] J. Liu, Z. Zhao, C. Xu, A. Duan, Appl. Catal. B 78 (2008) 61–72.
[20] P.G. Harrison, I.K. Ball, W. Daniell, P. Lukinskas, M. Céspedes, E.E. Miró, M.A. Ulla, Chem. Eng. J. 95 (2003) 47–55.
[21] H.-H. Kim, Plasma Process. Polym. 1 (2004) 91–110.
[22] A.M. Vandenbroucke, R. Morent, N. De Geyter, C. Leys, J. Hazard. Mater. 195 (2011) 30–54.
[23] S. Thomas, A. Martin, D. Raybone, J. Shawcross, K.A. Ng, P. Beech, J.C. Whitehead, Non thermal plasma aftertreatment of particulates—theoretical limits and impact on reactor design, in: International Spring Fuels and Lubricants Meeting and Exposition, SAE Technical Papers 2000, Paris, France, 2001.
[24] J.S. Chang, P.A. Lawless, T. Yamamoto, IEEE Trans. Plasma Sci. 19 (1991) 1152–1166.
[25] J. Jarrige, P. Vervisch, J. Appl. Phys. 99 (2006) 113303.
[26] B. Eliasson, M. Hirth, U. Kogelschat, J. Phys. D: Appl. Phys. 20 (1987) 1421–1437.
[27] J.V. Durme, J. Dewulf, C. Leys, H.V. Langenhove, Appl. Catal. B 78 (2008) 324–333.
[28] A. Baylet, P. Marécot, D. Duprez, X. Jeandel, K. Lombaert, J. Tatibouët, Appl. Catal. B 113 (2012) 31–36.
[29] A. Maciuca, C. Batiot-Dupeyrat, J.-M. Tatibouët, Appl. Catal. B 125 (2012) 432–438.

[30] J. Van Durme, J. Dewulf, W. Sysmans, C. Leys, H. Van Langenhove, Appl. Catal. B 74 (2007) 161–169.
[31] S. Yao, S. Yamamoto, S. Kodama, C. Mine, Y. Fujioka, Open Catal. J. 2 (2009) 79–85.
[32] C. Barakat, P. Gravejat, O. Guaitella, F. Thevenet, A. Rousseau, Appl. Catal. B 147 (2014) 302–313.
[33] M. Khoudiakov, M.C. Gupta, S. Deevi, Appl. Catal. A 291 (2005) 151–161.
[34] M. Gálvez, S. Ascaso, P. Stelmachowski, P. Legutko, A. Kotarba, R. Moliner, M. Lázaro, Appl. Catal. B 152 (2014) 88–98.
[35] J.P. Neeft, M. Makkee, J.A. Moulijn, Appl. Catal. B 8 (1996) 57–78.
[36] S. Yao, Recent Pat. Chem. Eng. 2 (2009) 67–75.
[37] H. Lin, Z. Huang, W. Shangguan, Chem. Eng. Technol. 31 (2008) 110–115.
[38] H. Hayashi, K. Takashima, A. Mizuno, Int. J. Plasma Environ. Sci. Tech. 6 (2012) 160–165.
[39] M.T. Nguyen Dinh, J.-M. Giraudon, J.-F. Lamonier, A. Vandenbroucke, N. De Geyter, C. Leys, R. Morent, Appl. Catal. B 147 (2014) 904–911.
[40] M. Hołub, S. Kalisiak, T. Borkowski, J. Myśków, R. Brandenburg, Pol. J. Environ. Stud. 19 (2010) 1199–1211.
[41] M. Okubo, T. Kuroki, K. Yoshida, T. Yamamoto, IEEE Trans. Ind. Appl. 46 (2010) 2143–2150.
[42] S. Yao, E. Suzuki, A. Nakayama, J. Hazard. Mater. 83 (2001) 237–242.
[43] S. Wagloehner, M. Nitzer-Noski, S. Kureti, Chem. Eng. J. 259 (2015) 492–504.
[44] Y. Lou, L. Wang, Z. Zhao, Y. Zhang, Z. Zhang, Appl. Catal. B 146 (2014) 43–49.
[45] C.-W. Tang, C.-B. Wang, S.-H. Chien, Thermochim. Acta 473 (2008) 68–73.
[46] A. Basinska, W.K. Józwiak, J. Góralski, F. Domka, Appl. Catal. A 190 (2000) 107–115.
[47] M. Iwamoto, Y. Yoda, N. Yamazoe, T. Seiyama, J. Phys. Chem. 82 (1978) 2564–2570.
[48] S. Maghsoodi, J. Towfighi, A. Khodadadi, Y. Mortazavi, Chem. Eng. J. 215-216 (2013) 827–837.
[49] N. Guilhaume, B. Bassou, G. Bergeret, D. Bianchi, F. Bosselet, A. Desmartin-Chomel, B. Jouguet, C. Mirodatos, Appl. Catal. B 119–120 (2012) 287–296.
[50] K. Ramesh, L. Chen, F. Chen, Y. Liu, Z. Wang, Y.-F. Han, Catal. Today 131 (2008) 477–482.
[51] S. Yamamoto, S. Yao, S. Kodama, C. Mine, Y. Fujioka, Open Catal. J. 1 (2008) 11–16.
[52] C. Subrahmanyam, A. Renken, L. Kiwi-Minsker, Chem. Eng. J. 134 (2007) 78–83.
[53] J. Van Durme, J. Dewulf, K. Demeestere, C. Leys, H. Van Langenhove, Appl. Catal. B: Environ. 87 (2009) 78–83.
[54] A.M. Vandenbroucke, M. Mora, C. Jiménez-Sanchidrián, F.J. Romero-Salguero, N. De Geyter, C. Leys, R. Morent, Appl. Catal. B 156–157 (2014) 94–100.
[55] S. Yao, C. Fushimi, K. Madokoro, K. Yamada, Plasma Chem. Plasma Process. 26 (2006) 481–493.
[56] S. Yao, M. Okumoto, T. Yashima, J. Shimogami, K. Madokoro, E. Suzuki, AIChE J. 50 (2004) 715–721.
[57] X. Tang, H. Lu, L. Lin, S. Yao, Plasma Chem. Plasma Process. 33 (2013) 281–292.
[58] S.Y. Park, B.R. Deshwal, S.H. Moon, Fuel Process. Technol. 89 (2008) 540–548.